MODELING OF HYDRAULIC FRACTURE PROPAGATION IN REAL HETERO-GENEOUS CONGLOMERATES FROM THE MAHU OILFIELD USING THE GLOBAL COHESIVE ZONE METHOD

Mingyang Zhang [1#] ID, Yanying Chen [2#] ID, Ming Yue [2] ID, Ninghong Jia [3] ID, Weifeng Lyu [3] ID, Amer Alizadeh [4] ID, Haoran Cheng [5,6] ID, Chiyu Xie [*1,7,8] ID

[1] School of Astronautics, Beihang University, Beijing, China; [2] School of Civil and Resource Engineering, University of Science and Technology Beijing, Beijing, China; [3] Research Institute of Petroleum Exploration and Development, PetroChina, Beijing, China; [4] College of Engineering and Physical Sciences, University of Birmingham, Birmingham, UK; [5] Sichuan Energy Internet Research Institute Tsinghua University, Chengdu, Sichuan, China; [6] School of Chemical Engineering, Qingdao University of Science and Technology, Qingdao, Shandong, China; [7] State Key Laboratory of High-Efficiency Reusable Aerospace Transportation Technology, Beijing, China; [8] Ningbo Institute of Technology, Beihang University, Ningbo, China

[#] These authors contributed equally to the work

ABSTRACT

Hydraulic fracturing enhances production in unconventional reservoirs but is challenged by reservoir heterogeneity, which complicates fracture propagation and reduces the efficiency of conglomerate reservoir development. The Mahu area in Xinjiang, a major petroleum reservoir in western China, is rich in oil and gas but features highly heterogeneous geological structures that complicate hydraulic fracturing and hydrocarbon extraction. In this study, we analyzed both homogeneous and heterogeneous core samples from the Mahu area. Real pore structures and gravel compositions were obtained using Computed Tomography (CT) and Quantitative Evaluation of Minerals by Scanning Electron Microscopy (QEMSCAN). The Global Pore-Pressure Cohesive Zone (GPPCZ) model was applied to study the impact of heterogeneity on fracture propagation, considering differences in the mechanical properties of the matrix, gravel, and interfaces. Results showed that fractures tend to propagate in regions with lower critical fracture energy. In heterogeneous cores, fractures were more likely to deflect around gravel and bifurcate, forming complex networks. Peak propagation velocity occurred at interface contacts, but homogeneous cores exhibited faster propagation under the same stress conditions. This work provides theoretical support for optimizing hydraulic fracturing strategies in heterogeneous conglomerate reservoirs such as the complex Mahu area.

1. INTRODUCTION

The consumption of oil and gas resources in China is steadily increasing. As conventional reservoirs enter their mid-to-late development stages (2), the exploitation of unconventional reservoirs has become crucial for addressing global energy challenges (7). Conglomerate reservoirs, with their high porosity and permeability, are emerging as a key focus of unconventional oil and gas resource development. However, the current exploitation of conglomerate reservoirs faces challenges such as low recovery rates and poor economic returns. For instance, the recovery rate of the Bakken conglomerate reservoir in the United States is approximately 10% to 15% (32), while that of the Mahu area oilfields in Xinjiang, China, is about 10% to 20% (18, 45). Hydraulic fracturing is a commonly employed technique for developing conglomerate reservoirs (22), but the strong heterogeneity of conglomerates complicates the evaluation of hydraulic fracturing performance, significantly limiting extraction efficiency (40, 48, 50).

Characterizing the heterogeneity of conglomerates and understanding its influence on flow behavior are key to addressing this challenge. Researchers primarily describe heterogeneity by analyzing the structural features of conglomerates and assigning mechanical properties to gravels. Existing studies on hydraulic fracturing simulations in conglomerate reservoirs often simplify gravels as circular structures with uniform diameters (4, 34). This approach is commonly used to investigate the impact of factors such as stress differences and injection rates on hydraulic fracture propagation.

Conglomerates typically form in high-energy depositional environments and are often irregular in shape (10, 39). Studies have shown that gravel size (17), shape (30), interface strength, and mechanical properties (44) significantly influence the propagation patterns of hydraulic fractures. Therefore, incorporating the realistic structural features of conglomerates is crucial for accurate numerical simulations of hydraulic fracturing.

Pan et al. (26) modeled the conglomerates in the Mahu area using circular gravels of varying diameters (ranging from 20 mm to 40 mm) to represent the heterogeneity of the conglomerates in the reservoir. Their results demonstrate that the propagation path of hydraulic fractures is jointly influenced by the properties of the interfaces and gravels. When interface strength exceeds 40% of the matrix strength, hydraulic fractures are more likely to penetrate the gravel. Conversely, when gravel strength is higher than matrix strength, hydraulic fractures stop propagating after entering the gravel. Cao et al. (3) modeled gravels as irregular polygons of varying sizes, revealing that the combined effects of interfaces and gravels in conglomerates alter hydraulic fracture propagation paths. They emphasized that neglecting interface influences in simulations reduces the accuracy of hydraulic fracture predictions. However, these studies often simplify gravel characteristics, failing to capture the true complexity of heterogeneous conglomerate structures. Additionally, they do not rigorously consider how variations in the mechanical properties of different gravels affect fracture propagation. Shi et al. (31) compared numerical simulations of hydraulic fracturing between a homogeneous conglomerate model with uniformly sized gravels and the heterogeneous conglomerate model with composite gravels, concluding that the latter exhibits more microfractures. Zhu et al. (55, 56) used a Coupled Discrete Element-Lattice Boltzmann Method to simulate the hydraulic fracturing process considering the interaction between natural and hydraulic fractures. Their results indicated that hydraulic fractures tend to propagate toward natural fractures with lower strength, which fail due to stress variations and subsequently form localized clusters. Current research on the mechanisms of hydraulic fracture propagation in heterogeneous conglomerates remains limited, particularly regarding the incorporation of real core structures, gravel shapes, and mechanical properties. These factors significantly influence fracture morphology.

Therefore, this study investigates fracture propagation in two real conglomerate cores from the Mahu area oilfield using a finite element model based on the Global Pore-Pressure Cohesive Zone Element (GPPCZ) method. The fracture propagation process and morphology in homogeneous and heterogeneous conglomerates are compared and analyzed. In Section 2, digital core models of homogeneous and heterogeneous cores from the Mahu area are constructed using Computed Tomography (CT) and Quantitative Evaluation of Minerals by Scanning Electron Microscopy (QEMSCAN). The gravel structures, types, and mechanical properties of various gravels are obtained. In Section 3, the implementation of the coupled poroelasticity equations for porous media and the GPPCZ method is detailed, and its accuracy is validated through comparisons with existing research findings. In Section 4, the GPPCZ model is applied to the real core models for hydraulic fracturing simulations, providing insights into the impact of conglomerate heterogeneity on hydraulic fracture propagation.

2. DATA AND INTERPRETATION

2.1. Geological description

The Mahu area, situated in the northwest region of the Junggar Basin, represents a prominent example of a conglomerate oil reservoir characterized by highly heterogeneous reservoir structures (14, 16). Based on recent drilling data, the burial depth of deep reservoirs in this region ranges from 4500 and 5300 meters, with an average depth of approximately 4755 meters. Vertically, the reservoirs span multiple Permian formations, from the Jiamaohe Formation in the Lower Permian to the Wuerhe Formation in the Upper Permian. Horizontally, these reservoirs are extensively distributed across the southern part of the Mahu Depression and its uplift regions (12).

The deep, tight conglomerate reservoirs in the Mahu area are predominantly composed of fine and medium-fine conglomerates, with gravel sizes ranging from 2 mm × 3 mm to 9 mm × 10 mm. Medium conglomerates are widely distributed and represent the primary reservoir rocks in the Mahu area, with gravel sizes ranging from 10 mm × 12 mm to 46 mm × 52 mm. Coarse conglomerates, featuring gravel sizes exceeding 50 mm × 52 mm, are relatively rare (33).

These reservoirs are characterized by highly uneven gravel distributions, with significant variations in gravel size, shape, and mechanical properties. These differences result in pronounced spatial heterogeneity in the reservoirs' pore structure and permeability. Additionally, the mechanical properties at the interfaces between the gravel and the matrix vary with depths and locations, complicating the generation and propagation of fractures during hydraulic fracturing (35). This heterogeneous structure makes predicting fracture propagation paths challenging, as they are highly influenced by the position and mechanical properties of the gravel. Under such complex conditions, advanced and precise
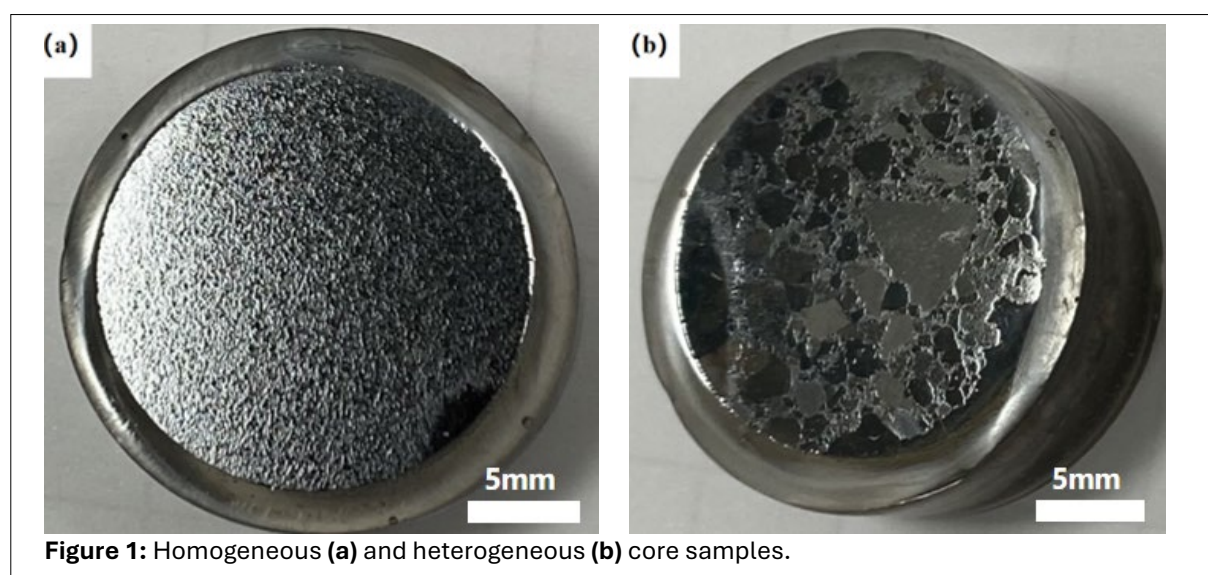

Figure 1: Homogeneous **(a)** and heterogeneous **(b)** core samples.

technologies are required to effectively control fracture morphology, thereby enhancing hydrocarbon recovery and improving reservoir development performance.

2.1.   The characteristics of core samples

We selected two core samples from the Mahu area in Xinjiang for analysis (as shown in **Fig. 1**). Both core samples have dimensions of 25 × 50 mm, which are about 50 times larger than the mean gravel diameter of the Mahu conglomerates, according to the data reported by Sun et al. (33). The core slice shown in **Figure 1a** exhibits high homogeneity, with a uniform mineral distribution and almost no discernible gravel structures. In contrast, the core slice in **Figure 1b** displays significant heterogeneity, featuring gravel structures of varying sizes and shapes, highlighting the sample's heterogeneous nature.

2.2. CT results

To accurately identify and characterize the pore structures and skeletal features of the core samples, CT scanning analyses were conducted on both heterogeneous and homogeneous core samples in this study (53). The two cores exhibit markedly different internal structural characteristics. Using CT scanning with a resolution of 14.8 μm, a total of 1,751 two-dimensional slice images were obtained.

The CT scan results of the homogeneous core (**Fig. 2a**) reveal a uniform internal structure, with no observable gravel or other heterogeneous features. The pore structure is relatively simple. In contrast, the heterogeneous core (**Fig. 2b**) displays prominent gravel structures of varying sizes and shapes, distributed unevenly throughout the core. This results in a complex pore network and irregular particle arrangements, indicating a high degree of heterogeneity. By comparing the structural characteristics of these two core samples, we gain deeper insights into the structural heterogeneity differences between the two core types, providing a solid foundation for subsequent numerical simulations.
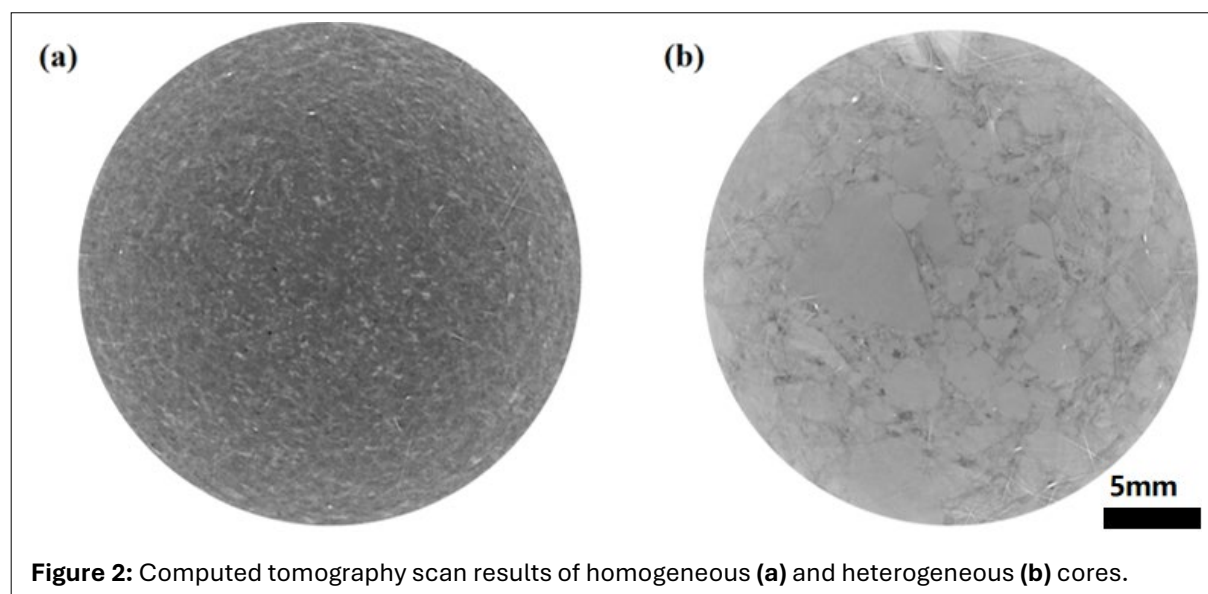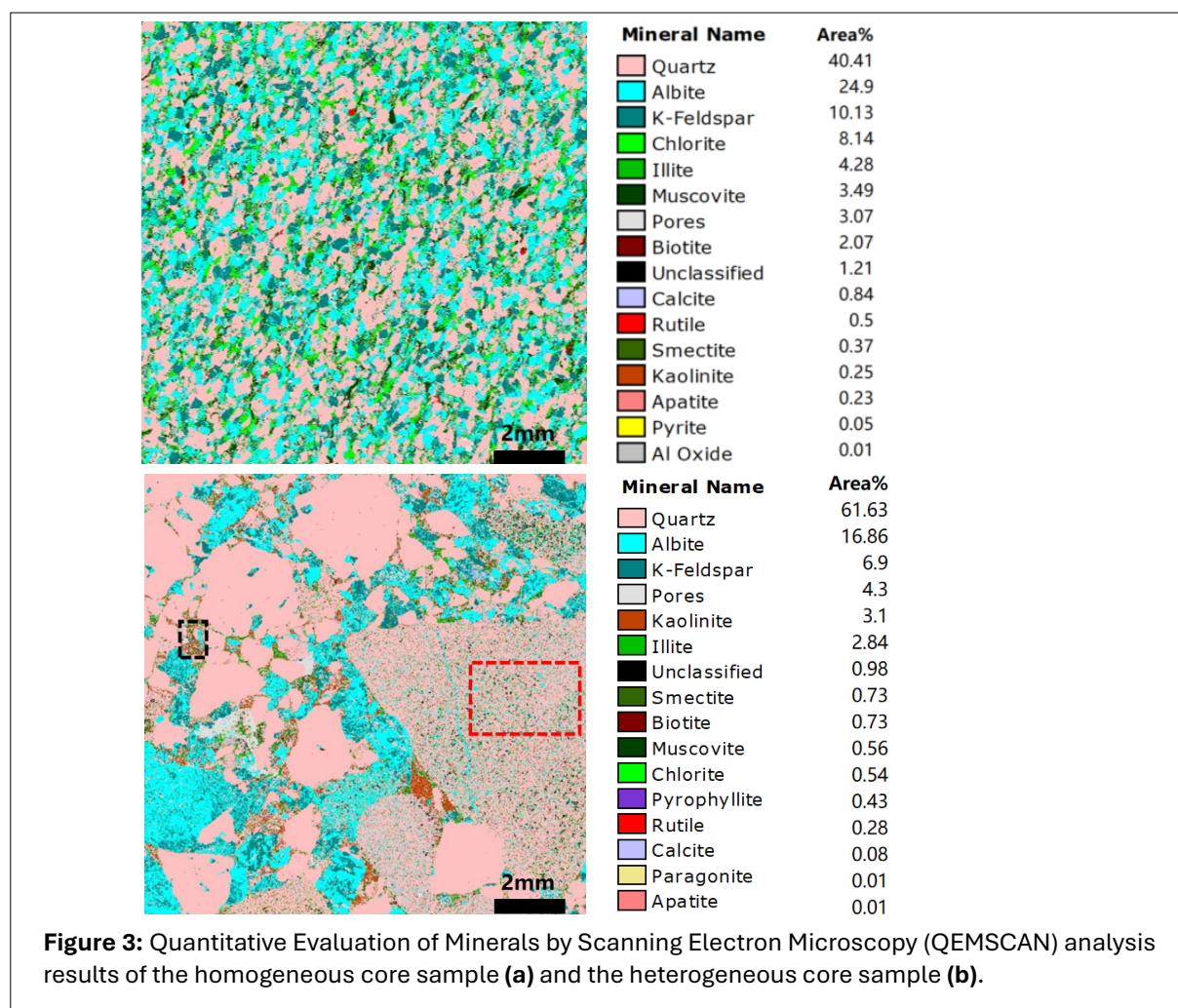

Figure 2: Computed tomography scan results of homogeneous **(a)** and heterogeneous **(b)** cores.

The CT scan images of the homogeneous and heterogeneous cores are reconstructed into three-dimensional (3D) digital core models. Quantitative analysis of the 3D pore models reveals that the porosity of the homogeneous core is 0.141, while that of the heterogeneous core is 0.097.

2.3.   QEMSCAN results

To further analyze the mineral content proportions and distribution characteristics of the homogeneous and heterogeneous cores, the QEMSCAN technique was employed to characterize the mineral properties of the two core samples. The use of QEMSCAN provides precise mineral identification and reliable quantitative analysis (41). The QEMSCAN results for the homogeneous core (**Fig. 3a**) indicate quartz (40.41%) and albite (24.9%) contents, which are evenly distributed with no evidence of mixed gravel structures.

Figure 3: Quantitative Evaluation of Minerals by Scanning Electron Microscopy (QEMSCAN) analysis results of the homogeneous core sample **(a)** and the heterogeneous core sample **(b)**.

The QEMSCAN results for the heterogeneous core (**Fig. 3b**) reveal a complex mineral composition, with quartz (61.63%) and albite (16.86%) being the dominant minerals, forming a complex gravel structure primarily composed of these two minerals. The heterogeneous core also contains mixed gravel structures, including quartz-albite-illite mixed gravels (highlighted in red boxes) and illite-kaolinite mixed gravels (highlighted in black boxes). The mechanical properties of mixed gravels are defined as the average values of their constituent minerals. The QEMSCAN analysis further highlights the significant differences in mineral composition and internal structure between the homogeneous and heterogeneous cores, as well as the impact of these differences on numerical simulations.

By integrating the results of CT scanning and QEMSCAN analysis, we not only obtain the pore structure and characteristics of both heterogeneous and homogeneous cores but also accurately identify the mineral composition and its proportional distribution within the cores. This approach provides a precise basis for subsequent modeling, enabling the construction of physical models that accurately reflect the structural features of the two types of cores while incorporating the corresponding mineral types and physical properties.

3. NUMERICAL MODELING

3.1. Numerical approach

3.1.1. The cohesive element

The extended finite element method (XFEM) offers high precision with simple operations in hydraulic fracturing simulations; however, it may fail to converge when the rock is highly heterogeneous, and cannot simulate fracture bifurcation (9). The global pore pressure cohesive zone method (GPPCZ)

inherits the advantages of XFEM and is better suited for studying heterogeneity and fracture bifurcation (44).

The GPPCZ model describes the propagation of hydraulic fractures through the opening of cohesive elements. The failure process of cohesive elements follows the bilinear constitutive relationship shown in **Figure 4**, which consists of a linear elastic phase prior to the peak stress σ_{max} and a damage evolution phase thereafter. The cohesive element begins to fail when the separation distance δ_m^0 reaches a critical value and completely fails when the displacement reaches δ_m^f (20). The triangular area under the curve in **Figure 4** represents the critical fracture energy of the cohesive element (54). The bilinear constitutive relationship is applied as it provides the best compromise between computational efficiency and accuracy, although it is less precise than exact solutions (1).

Figure 4: Constitutive model of cohesive elements.
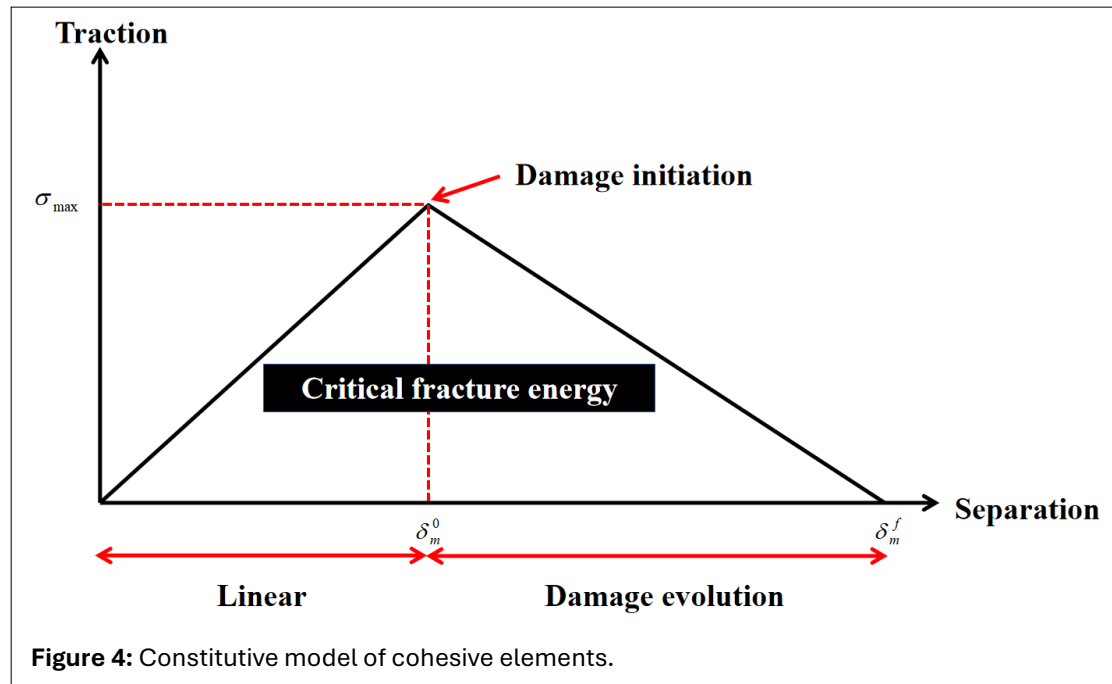
3.1.2. Criteria for fracture initiation and propagation

During the hydraulic fracturing process, cohesive elements are subjected to tensile and shear forces, resulting in the formation of mixed-mode hydraulic fractures. The traction-separation law of cracks under tensile and shear forces can be expressed as follows (42, 43; **Eq. 1**):

$$\begin{cases} \sigma_n = f_n(\delta_n) \\ \sigma_s = f_s(\delta_s) \end{cases} \tag{1}$$

where σ_n and σ_s are the normal and tangential traction stresses, respectively; δ_n and δ_s are the opening and shear displacements of the cohesive crack. f_n and f_s are functions that define the relationships between traction and separation under tensile and shear forces, respectively.

Before damage or crack initiation, the normal and tangential stresses increase linearly as a function of displacement according to a penalty stiffness, K_p, which can be expressed as follows (**Eq. 2**):

$$\begin{cases} \sigma_n = K_p \delta_n \\ \sigma_s = K_p \delta_s \end{cases} \tag{2}$$

Under such conditions, the fracture initiation criterion for cohesive elements is given as follows (5, 8, 15, 24; **Eq. 3**):

$$\left(\frac{\sigma_n}{\sigma_n^0}\right)^2 + \left(\frac{\sigma_s}{\sigma_s^0}\right)^2 = 1 \tag{3}$$

where σ_n^0 is the tensile strength of rock and σ_s^0 is the shear strength of rock.

The constitutive relationship for the cohesive element can be divided into two phases: the linear elastic phase and the damage evolution phase. The stress calculation equation is given by (46; **Eq. 4**):

$$\sigma = \begin{cases} (1-D)\overline{\sigma} & linear \\ \overline{\sigma} & damage \quad evolution \end{cases} \tag{4}$$

where, $\overline{\sigma}$ represents the stress value calculated during the linear elastic deformation phase, and D denotes the degree of damage. The values of D are 0 (undamaged) and 1 (completely damaged), respectively. According to the linear displacement expansion criterion, D can be expressed as (38; **Eq. 5**, **Eq. 6**):

$$D = \frac{\delta_m^f(\delta_m^{max_m^0}}{\delta_m^{max_{m_m}^{f^0}}} \tag{5}$$

$$\delta_m = \sqrt{\delta_n^2 + \delta_s^2 + \delta_t^2} \tag{6}$$

where δ_m represents the effective displacement; δ_n is the normal displacement component; δ_s and δ_t are the first and second shear displacement components, respectively; δ_m^0 is the displacement value when the element begins to fail; δ_m^{max} is the limit displacement value of the element, δ_m^f is the displacement value when the element begins to crack, as follows (**Eq. 7**):

$$\delta_m^f = \frac{2G^c}{T_{max}} \tag{7}$$

where T_{max} is the tensile strength or shear strength of the material, and G^c is the mixed mode fracture energy.

3.1.3. Damage evolution criterion

The critical fracture energy of mixed-mode fractures can be calculated using the Benzeggagh-Kenane (B-K) criterion (6, 29, 49; **Eq. 8**):

$$G_n^c + (G_s^c - G_n^c)\left(\frac{G_S}{G_T}\right)^\eta = G^C \tag{8}$$

where, G_n^c represents the critical strain energy release rate in the normal direction; G_s^c denotes the critical strain energy release rate in the first tangential direction; and G_S is the critical strain energy release rate in the shear direction. Additionally, G_T refers to the critical strain energy release rate in the tensile direction.

3.1.4. Fluid flow within fractures

As shown in **Figure 5**, the flow of fracturing fluid within hydraulic fractures can be categorized into two primary directions: **tangential flow** along the cohesive elements and **normal flow** perpendicular to the upper and lower surfaces of the cohesive elements. These two flow patterns collectively influence fracture propagation behavior. However, during fracture propagation, the tangential flow becomes the dominant factor due to its alignment with the fracture direction, thereby significantly impacting the effectiveness of hydraulic fracturing (21).

The flow characteristics of fracturing fluid within fractures can be described in terms of the pressure gradient and the local fracture width. During hydraulic fracturing, the mass conservation for the fracturing fluid can be expressed as follows (25, 52; **Eq. 9**):

$$\frac{dq_f}{dx} + q_t + q_b + \frac{dw}{dt} = 0 \tag{9}$$

In this model, q_f represents the average tangential flow velocity of the fluid along the fracture; q_t denotes fluid loss at the top surface of the fracture; q_b indicates fluid loss at the bottom surface; and w represents the fracture width. Additionally, the fracturing fluid flow is considered to be a combination of tangential and normal flow. Assuming the fluid is an incompressible Newtonian fluid, its tangential flow within the fracture can be described as follows (36; **Eq. 10**):
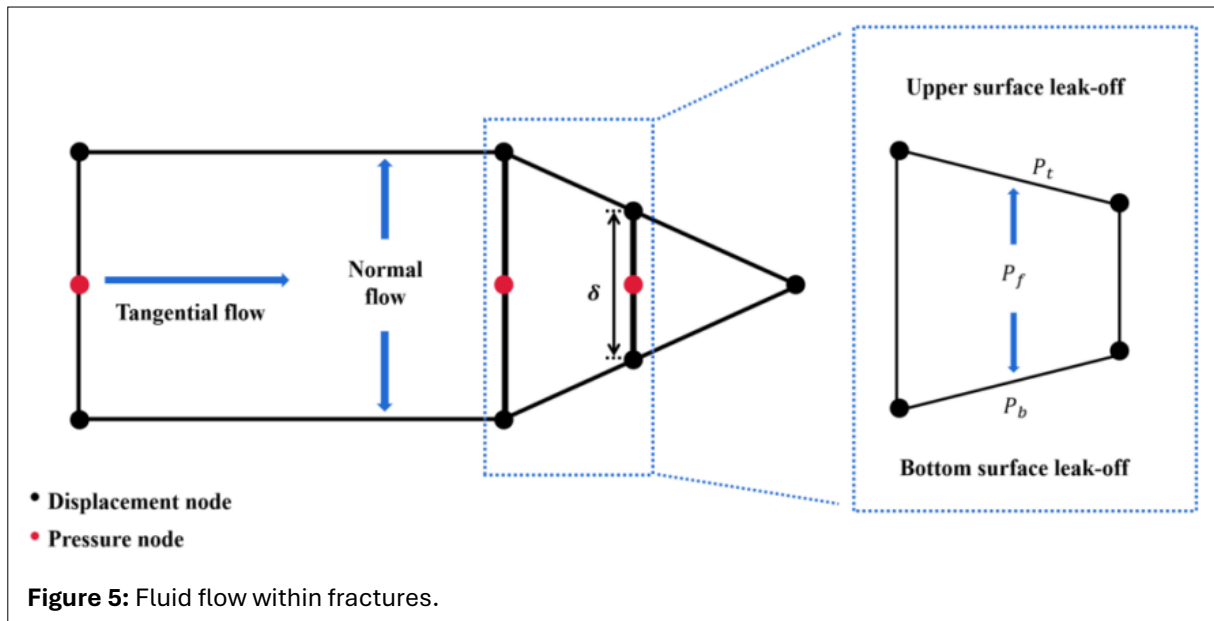
Figure 5: Fluid flow within fractures.

$$q_f = -\frac{w^3}{12\mu}\nabla p_f \tag{10}$$

where μ denotes the fluid viscosity, and ∇p_f represents the pressure gradient within the fracture. The leak-off rate of the fracturing fluid into the reservoir is governed by the leak-off coefficient of the surrounding medium. Based on the pressure-driven leak-off model, the relationship can be expressed as follows (37; **Eq. 11**):

$$\begin{cases} q_t = c_t(p_f - p_t) \\ q_b = c_b(p_f - p_b) \end{cases} \tag{11}$$

where p_t denotes the pressure at the top surface of the fracture, p_b represents the pressure at the bottom surface, and p_f is the fluid pressure within the fracture. p_t and p_b are calculated in Abaqus. c_t and c_b represent the pressure-dependent leak-off coefficients at the top and bottom surfaces of the fracture, respectively.

3.1.5. Global pore pressure cohesive element

The fracture width in hydraulic fracturing is calculated from the displacement difference between the upper and lower surfaces. Assuming that both displacements and fluid pressure vary linearly over the cohesive element, linear interpolation functions can be employed to determine the separation of the element and the fluid pressure at any location based on nodal values. Since the fracture width is computed using local nodal displacements, the global coordinates X of the cohesive element are first transformed into local coordinates x (19; **Eq. 12**):

$$x = RX \tag{12}$$

where R is the coordinate rotation matrix, which can be expressed as follows (**Eq. 13**):

$$R = \begin{bmatrix} \cos\theta & \sin\theta \\ -\sin\theta & \cos\theta \end{bmatrix} \tag{13}$$

where θ is the angle between the local and global coordinate system.

The transformation of global nodal displacements $\tilde{u}$ to local nodal displacements $\bar{u}$ is achieved through a coordinate system conversion (**Eq. 14**):

$$\tilde{u} = T\bar{u} \tag{14}$$

where $\bar{u} = (u_1, u_2, \ldots, u_7, u_8)^T$; T is the displacement transformation matrix, defined as (**Eq. 15**):

$$T = \begin{bmatrix} R & 0 & 0 & 0 \\ 0 & R & 0 & 0 \\ 0 & 0 & R & 0 \\ 0 & 0 & 0 & R \end{bmatrix} \tag{15}$$

The local nodal separation can be determined from the local nodal displacements, as follows (**Eq. 16**):

$$\tilde{\Delta} = L\tilde{u} \tag{16}$$

where L is the local displacement-separation relation matrix, which is defined as (**Eq. 17**):

$$L = \begin{bmatrix} -1 & 0 & 0 & 0 & 0 & 0 & 1 & 0 \\ 0 & -1 & 0 & 0 & 0 & 0 & 0 & 1 \\ 0 & 0 & -1 & 0 & 1 & 0 & 0 & 0 \\ 0 & 0 & 0 & -1 & 0 & 1 & 0 & 0 \end{bmatrix} \tag{17}$$

The separation fields can be determined as follows (**Eq. 18**):

$$\Delta(x) = N_w^T \tilde{\Delta} \tag{18}$$

where N_w is the interpolation function, which is defined as (**Eq. 19**):

$$N_w = \begin{bmatrix} \frac{l_e - \chi}{l_e} & 0 \\ 0 & \frac{l_e - \chi}{l_e} \\ \frac{\chi}{l_e} & 0 \\ 0 & \frac{\chi}{l_e} \end{bmatrix} \tag{19}$$

where l_e is the fracture length, and $\chi \in [0, l_e]$ is the location of the point of interest in the local coordinate system.

The relationship between the local separation field and global nodal displacement can be expressed as (**Eq. 20**):

$$\Delta(x) = B_c \bar{u} \tag{20}$$

where B_c is the global nodal displacement-separation relation matrix, $B_c = N_w^T LT$.

The width of the fracture can be expressed as follows (**Eq. 21**):

$$w(\chi) = N_1^T \Delta(x) = \begin{bmatrix} 0 \\ 1 \end{bmatrix}^T \Delta(x) \tag{21}$$

The fluid pressure is considered as traction acting on the internal surfaces of the failure GPPCZ element, which can be expressed as follows (**Eq. 22**):

$$p_f(\chi) = N_P^T P \tag{22}$$

where $p = (p_1, p_2)^T$ is the vector of fluid pressure, and N_P is the fluid pressure interpolation vector, which can be defined as (**Eq. 23**):

$$N_P = \begin{bmatrix} \frac{l_e - \chi}{l_e} \\ \frac{\chi}{l_e} \end{bmatrix} \tag{23}$$

The partial derivative of N_P with respect to the local coordinate χ is given as follows (**Eq. 24**):

$$M_P = \frac{\partial N_P}{\partial \chi} \tag{24}$$

3.1.6. Finite element formulation

The weak form of the equations governing the mechanical behavior of the GPPCZ elements can be derived using the principle of virtual work. The total virtual work done by internal forces on the surfaces

of internal components is equal to the work performed by external forces on the surfaces of external components (19; **Eq. 25**):

$$\int_{\Gamma c} \delta\Delta \cdot T_c \, dS - \int_{\Gamma c} \delta w(\chi) p_f (\chi) dS = \int_{\Gamma} \delta u \cdot T_{ext} dS \qquad (25)$$

where T_c is the sum of cohesive and friction tractions; Γ_c represents the internal element surfaces; T_{ext} denotes the external forces; Γ represents the external element surfaces; $\delta\Delta$, $\delta w(\chi)$, and δu are the virtual separation, virtual width, and virtual displacement, respectively.

The discrete form of **Equation 25** can be given as **Equation 26**:

$$\underbrace{(\int_{\Gamma c} B_c^T T_c dS) - (\int_{\Gamma c} B_c^T N_1 N_p^T dS) p}_{I_1} = \int_{\Gamma} N_w^T T_{ext} dS \qquad (26)$$

where p is the fluid pressure.

The weak form of the equations governing fluid flow behavior within the GPPCZ component is as follows (**Eq. 27**):

$$\int_{\Gamma c} \delta p_f \frac{\partial w}{\partial t} d\chi + \int_{\Gamma c} \frac{w^3}{12\mu} \frac{\partial p_f}{\partial \chi} \frac{\partial(\delta p_f)}{\partial \chi} d\chi = (\delta p_f q_0)|x = 0 \qquad (27)$$

The discrete form of **Equation 27** is given as **Equation 28**:

$$\underbrace{(\int_{\Gamma_c} N_p N_1^T B_c d\chi) \Delta\bar{u} + (\Delta t \int_{\Gamma_c} \frac{w^3}{12\mu} M_p M_p^T d\chi) p}_{I_2} = \Delta t (N_p q_0)|x = 0 \qquad (28)$$

where $\Delta\bar{u} = \bar{u} - \bar{u}_-$, and $\bar{u}_-$ is the nodal displacement vector at the end of the previous time step.

Combining **Equation 26** and **Equation 28**, the stiffness K and internal force f_{int} of this new GPPCZ element can be obtained as follows (**Eq. 29**, **Eq. 30**):

$$K = \begin{bmatrix} \dfrac{\partial I_1}{\partial \bar{u}} & \dfrac{\partial I_1}{\partial p} \\ \dfrac{\partial I_2}{\partial \bar{u}} & \dfrac{\partial I_2}{\partial_p} \end{bmatrix} \qquad (29)$$

$$f \begin{bmatrix} I_1 \\ I_2 \end{bmatrix}_{int} \qquad (30)$$

The above equations are solved using the finite element platform Abaqus 2021[a].

3.2. Validation

To validate the accuracy of the proposed model, a comparative analysis was performed between the numerical simulation results and the physical experimental data reported by Ma et al. (23). The relevant parameters used are listed in **Table 1**. **Figure 6a** shows the fracture propagation results from the physical experiment, while **Figure 6b** presents the corresponding numerical simulation results. **Figure 6c** illustrates the boundary conditions and mesh configurations used in the GPPCZ model method. To more clearly illustrate the fracture propagation paths, all numerical simulation results in this study have an amplified deformation scale of 70x for visualization purposes.
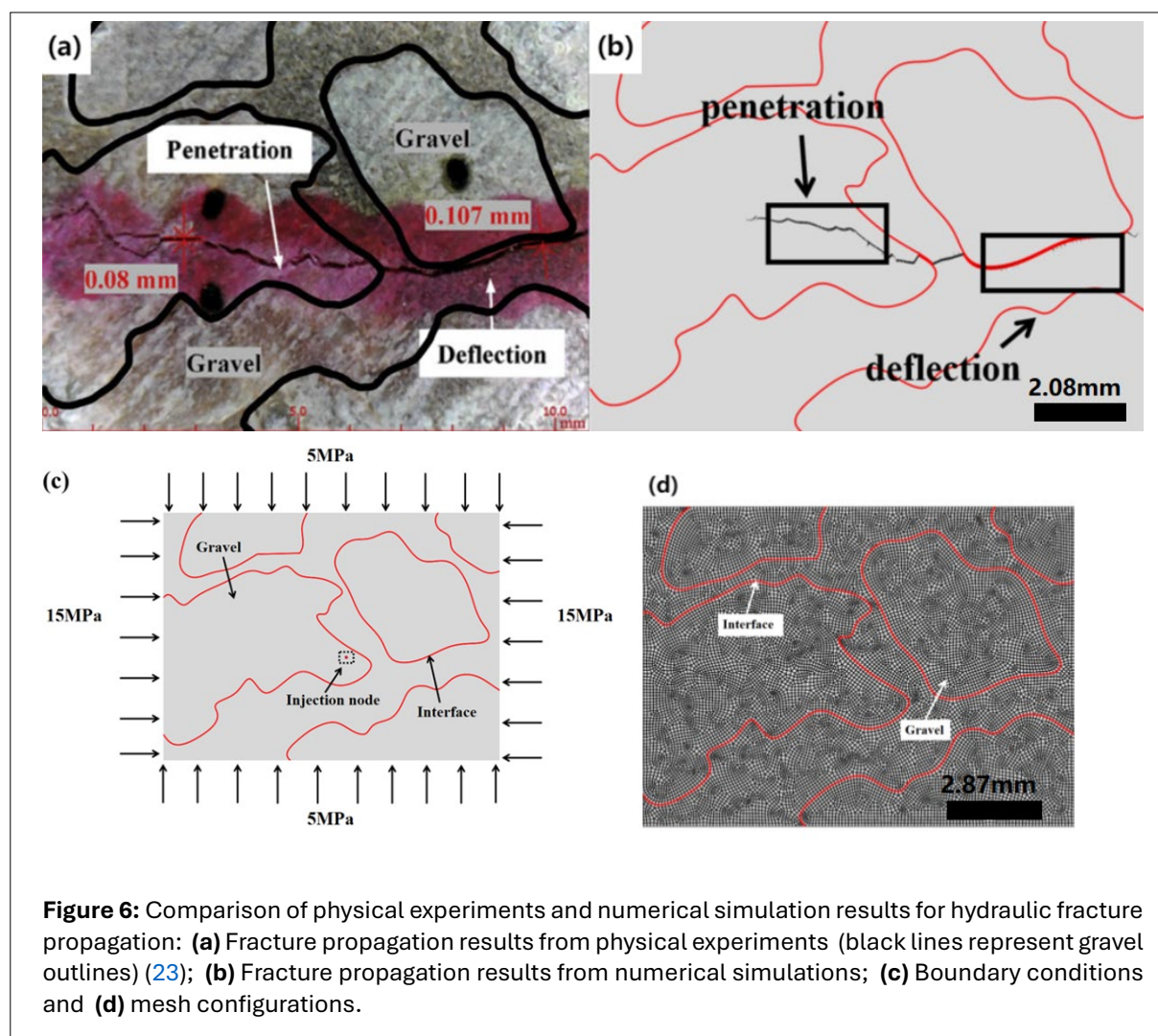
In both the physical experiment and numerical simulation, the fractures propagate along the direction of the maximum stress. Moreover, the numerical simulation accurately replicates the detailed behavior observed in the physical experiment. For instance, after a fracture penetrates a piece of gravel, it is attracted by another gravel during its propagation and extends along their interface. The comparison

---

[a] *https://www.suse.com/pcsc/viewVersionPage?versionID=21745*

between the physical experiment and numerical simulation results demonstrates that the numerical model is highly reliable.

Table 1: Parameters used in the physical experiment and numerical simulation.		
Parameters	**From literature (23)**	**Present simulation**
Young's modulus of matrix E_m (GPa)	36.7	36.7
Poisson's ratio of matrix ν_m	0.248	0.248
Tensile strength of matrix σ_m (MPa)	8.1	8.1
Shear strength of matrix τ_m (MPa)	-	20
Tensile fracture energy of matrix G_m^{IC} (J/$\mathbf{m^2}$)	-	1
Shear fracture energy of matrix G_m^{IIC} (J/$\mathbf{m^2}$)	-	80
Tensile strength of interface σ_i (MPa)	7.4	7.4
Shear strength of interface τ_i (MPa)	-	15
Tensile fracture energy of interface G_i^C (J/$\mathbf{m^2}$)	-	0.1
Shear fracture energy of interface G_i^{IIC} (J/$\mathbf{m^2}$)	-	20
Maximum horizontal stress (MPa)	15	15
Minimum horizontal stress (MPa)	5	5
Young's modulus of gravel E_r (GPa)	50.1	50.1
Poisson's ratio of gravel ν_r	0.247	0.247
Tensile strength of gravel σ_n^0 (MPa)	12.4	12.4
Shear strength of gravel σ_s^0 (MPa)	-	30
Tensile fracture energy of gravel G_r^C (J/$\mathbf{m^2}$)	-	5
Shear fracture energy of gravel G_r^{IIC} (J/$\mathbf{m^2}$)	-	100
Fluid viscosity μ (mPa-s)	120	120
Injection rate q (ml/min)	20	20
The dimensions of the model (m)	-	0.4 × 0.3
Porosity of matrix	-	0.1
Leak-off coefficient (m^3 /s/Pa)	-	1E-14

Figure 6: Comparison of physical experiments and numerical simulation results for hydraulic fracture propagation: **(a)** Fracture propagation results from physical experiments (black lines represent gravel outlines) (23); **(b)** Fracture propagation results from numerical simulations; **(c)** Boundary conditions and **(d)** mesh configurations.

4. RESULTS AND DISCUSSION

4.1. Numerical setup

We selected two portions of the core structures from **Figure 3** for the fracturing modeling, as shown in **Figure 7**, representing the homogeneous and heterogeneous cases, respectively. The selected regions ensure the primary structural features and mineral components of the core samples to be captured.

The numerical setups for the homogeneous and heterogeneous core models are illustrated in **Figure 8a** and **8b**, respectively, with the stress boundary conditions and water injection points also shown. The mechanical parameters used in the simulations are based on the actual mineral composition of the cores. The simulation parameters (11, 13, 27, 28, 47, 51) are listed in **Table 2** and **Table 3**, respectively, for the homogeneous and heterogeneous core models.

We investigate the impact of conglomerate heterogeneity on hydraulic fracture morphology, with two groups of stress differences being considered. In Section 4.2, the effects of heterogeneity on hydraulic fracture morphology are discussed. In Section 4.3, the fracture lengths and propagation velocities of homogeneous and heterogeneous core models are compared.
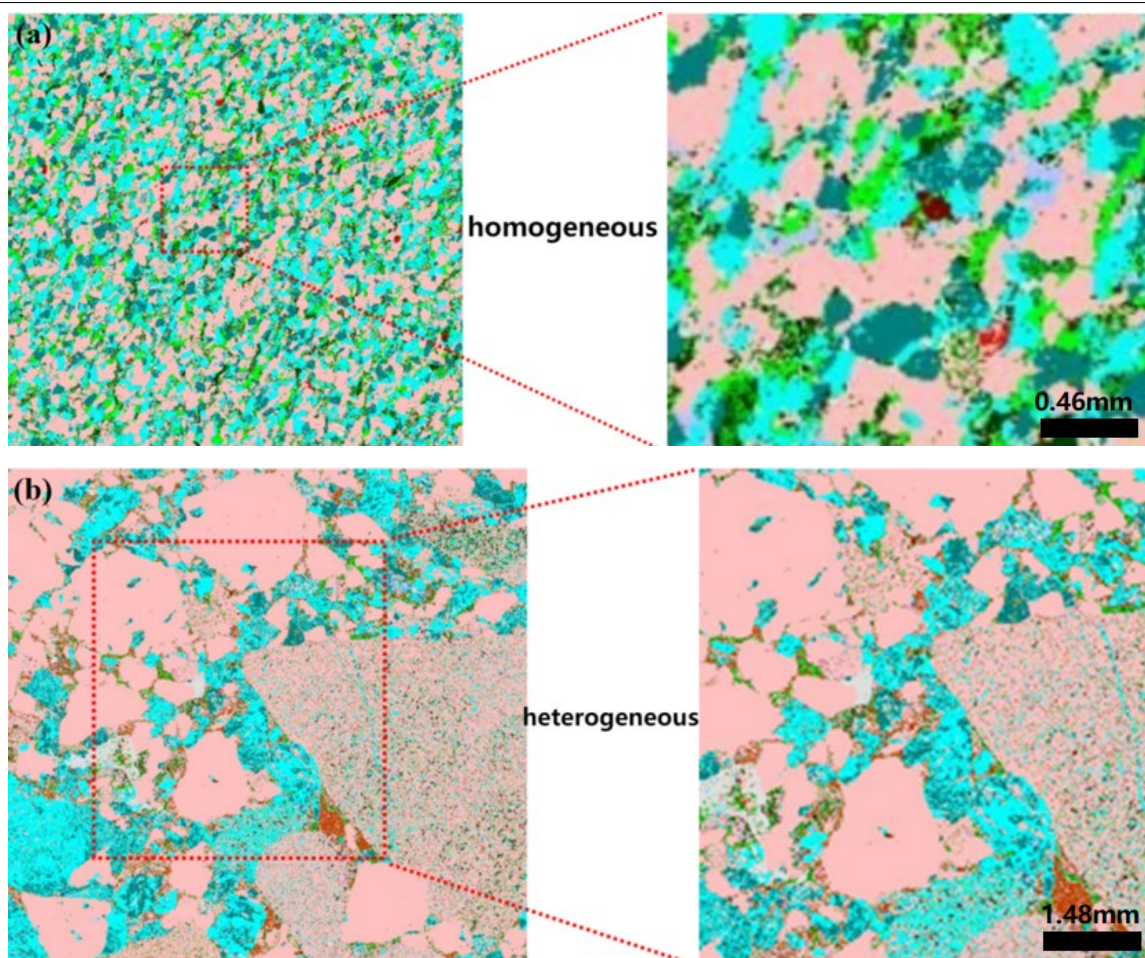
Figure 7: The selected portion for the fracturing modeling in **(a)** the homogeneous core sample; and **(b)** the heterogeneous core sample. The mineral components include quartz (pink), albite (blue), illite (green), kaolinite (orange), quartz-albite-illite mixed gravel (purple), and illite-kaolinite mixed gravel (yellow).
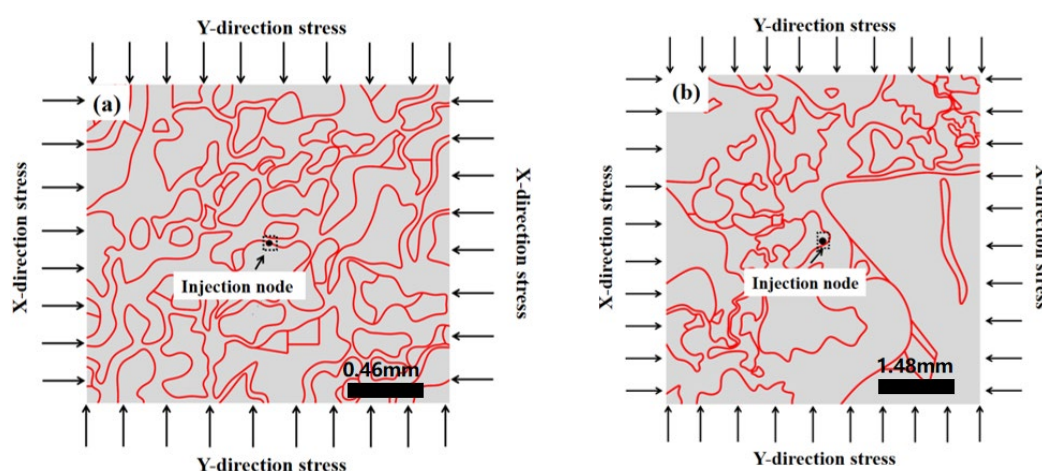

Figure 8: The numerical set-ups for **(a)** the homogeneous; and **(b)** the heterogeneous core models.

Table 2: Simulation parameters for the homogeneous core model.

Mineral Name	Material	Young's Modulus /GPa	Poisson's Ratio	Tensile strength /Mpa	Shear strength /MPa	Tensile fracture energy/(J/㎡)	Shear fracture energy/ (J/㎡)
Quartz	Gravel	95	0.07	12	120	4	1000
Albite	Gravel	69	0.28	8	80	2.67	667.5
	Interface	-	-	4	40	0.08	80
K-feldspar	Gravel	91.78	0.28	2	20	0.67	167.5
	Interface	-	-	1	10	0.02	20
chlorite	Gravel	38.9	0.2	12	120	4	1000
	Interface	-	-	6	60	0.12	120

Table 3: Simulation Parameters for the Heterogeneous Core Model.

Mineral Name	Material	Young's Modulus /GPa	Poisson's Ratio	Tensile strength /Mpa	Shear strength /MPa	Tensile fracture energy/ (J/㎡)	Shear fracture energy/ (J/㎡)
Quartz	Gravel	95	0.07	12	120	4	1000
Illite	Gravel	43.88	0.236	2.16	21.6	0.72	180
	Interface	-	-	1.08	10.8	0.0216	21.6
Kaolinite	Gravel	120	0.24	10.6	106	3.53	882.5
	Interface	-	-	5.3	53	0.106	106
Albite	Gravel	69	0.28	8	80	2.67	667.5
	Interface	-	-	4	40	0.08	80
Quartz-albite-illite mixed gravel	Gravel	69.29	0.195	7.39	73.9	2.46	615
	Interface	-	-	3.695	36.95	0.0739	73.9
Illite-kaolinite mixed gravel	Gravel	81.94	0.238	6.38	63.8	2.13	532.5
	Interface	-	-	3.19	31.9	0.0638	63.8

4.2. Comparisons of fracture Morphology

4.2.1. Comparison of fracture morphologies under a stress difference of 10 MPa
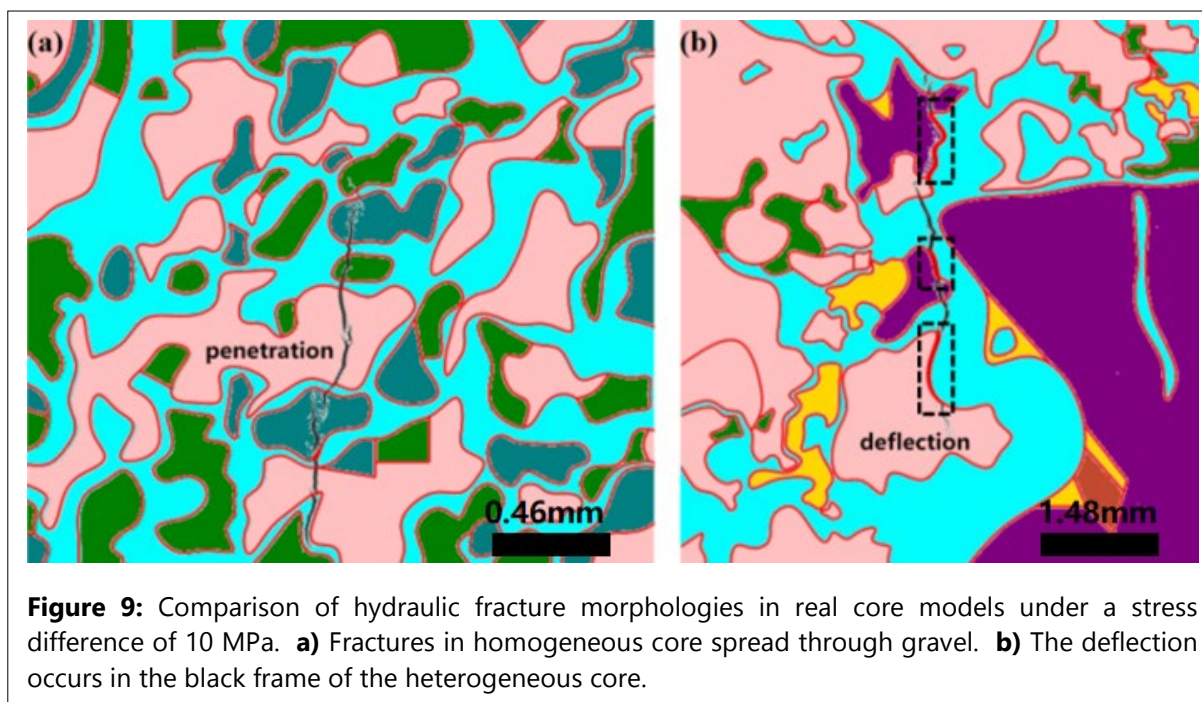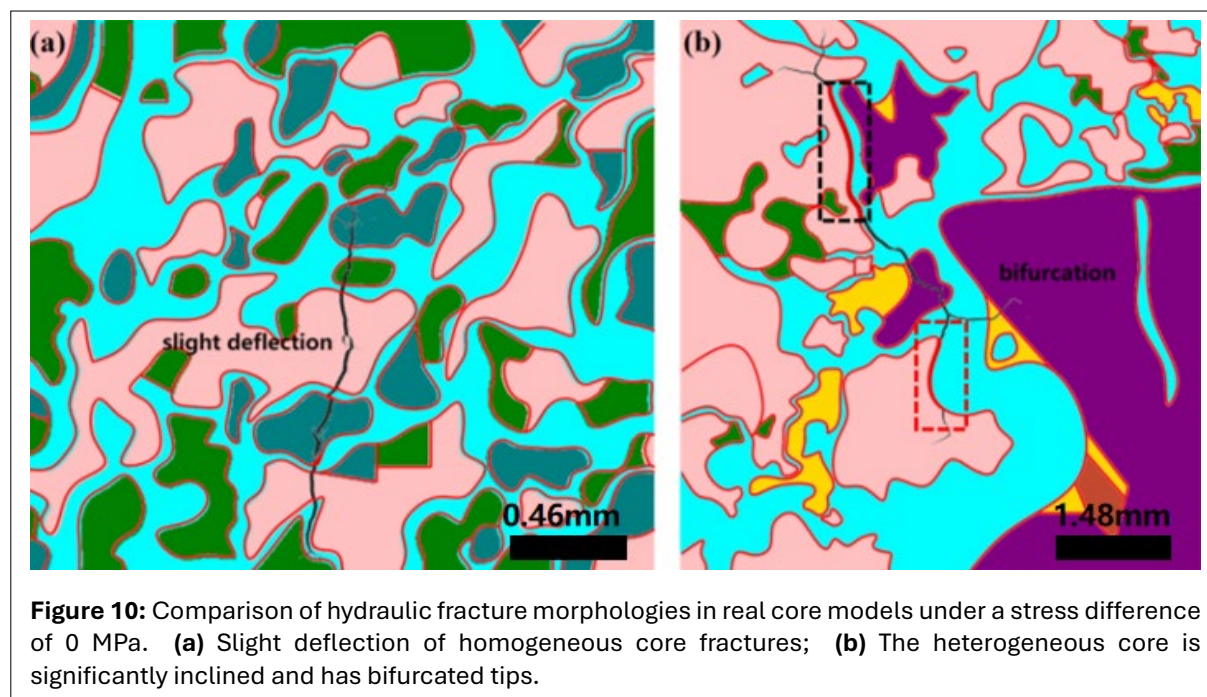
This section investigates the influence of heterogeneity on hydraulic fracture morphology by comparing the propagation paths of hydraulic fractures in homogeneous and heterogeneous real core models, under a horizontal stress difference of 10 MPa. The corresponding simulation parameters are presented in **Table 4**.

Table 4: Simulation parameters under a stress difference of 10 MPa.

Fluid viscosity / (mPa·s)	X-direction stress /MPa	Y-direction stress /MPa	Injection rate /(L/s)
120	0	10	0.001

Figure 9 illustrates the propagation paths of hydraulic fractures in homogeneous and heterogeneous real core models under a stress difference of 10 MPa.

The simulation results show that fractures in the homogeneous core model (**Fig. 9a**) propagate entirely through penetration, while fractures in the heterogeneous core model exhibit deflection at three locations (highlighted by black boxes in **Fig. 9b**). These findings indicate that the heterogeneity of conglomerates significantly influences the propagation paths of hydraulic fractures. Notably, fracture deflection behavior is more pronounced at the interfaces within the heterogeneous core model. Therefore, the propagation of hydraulic fractures is strongly governed by the internal structural heterogeneity of the conglomerate reservoirs, which has important implications for the effectiveness of hydraulic fracturing and fracture design.

Figure 9: Comparison of hydraulic fracture morphologies in real core models under a stress difference of 10 MPa. **a)** Fractures in homogeneous core spread through gravel. **b)** The deflection occurs in the black frame of the heterogeneous core.

4.2.2. Comparison of fracture morphologies under a stress difference of 0 MPa

This section investigates the influence of structural heterogeneity on hydraulic fracture morphology by comparing the propagation paths of hydraulic fractures in homogeneous and heterogeneous real core models under a horizontal stress difference of 0 MPa. The corresponding parameters are presented in **Table 5**.

Table 5: Simulation parameters under a stress difference of 0 MPa.

Fluid viscosity / (mPa·s)	X-direction stress /MPa	Y-direction stress /MPa	Injection rate / (L/s)
120	10	10	0.001

Figure 10 illustrates the propagation paths of hydraulic fractures in homogeneous and heterogeneous real core models under a stress difference of 0 MPa. The simulation results clearly show that the fracture propagation path in the homogeneous conglomerate (**Fig. 10a**) exhibits slight local deflection but remains generally straight, with no evidence of deflection or bifurcation. In contrast, the hydraulic fractures in the heterogeneous core model (**Fig. 10b**) display noticeable inclination and bifurcation at the fracture tip. In the regions highlighted by black and red boxes in **Figure 10b**, the fractures deflect along the quartz-albite interfaces. This occurs because the tensile fracture energy of the quartz-albite interface is lower than that of albite, causing the hydraulic fractures to preferentially propagate through areas with lower tensile fracture energy. The differences that are observed in the simulation results of **Figure 10** can be attributed to the larger gravel sizes in the heterogeneous core. When the fracture encounters gravel with higher tensile fracture energy, it cannot penetrate directly but instead deflects along the gravel interface, ultimately leading to bifurcation of the fracture path. Moreover, larger gravel acts as a point of discontinuity, distorting the surrounding stress field and inducing stress concentration effects. When the fracture tip reaches these localized stress concentration regions, the fracture path may deflect, resulting in multidirectional bifurcation phenomena.

The numerical simulation results from **Figure 9** and **Figure 10** collectively demonstrate that the shape and mechanical properties of gravel in conglomerates significantly influence fracture propagation paths during hydraulic fracturing. In heterogeneous cores, hydraulic fractures are more likely to exhibit deflection and bifurcation, with the fracture paths typically favoring regions of lower tensile fracture energy. These deflection patterns are in accordance with the field observations (57) that "HF opens in the direction of least principal stress and rapidly propagates in the plane containing the largest and intermediate principal stress".

Figure 10: Comparison of hydraulic fracture morphologies in real core models under a stress difference of 0 MPa. **(a)** Slight deflection of homogeneous core fractures; **(b)** The heterogeneous core is significantly inclined and has bifurcated tips.
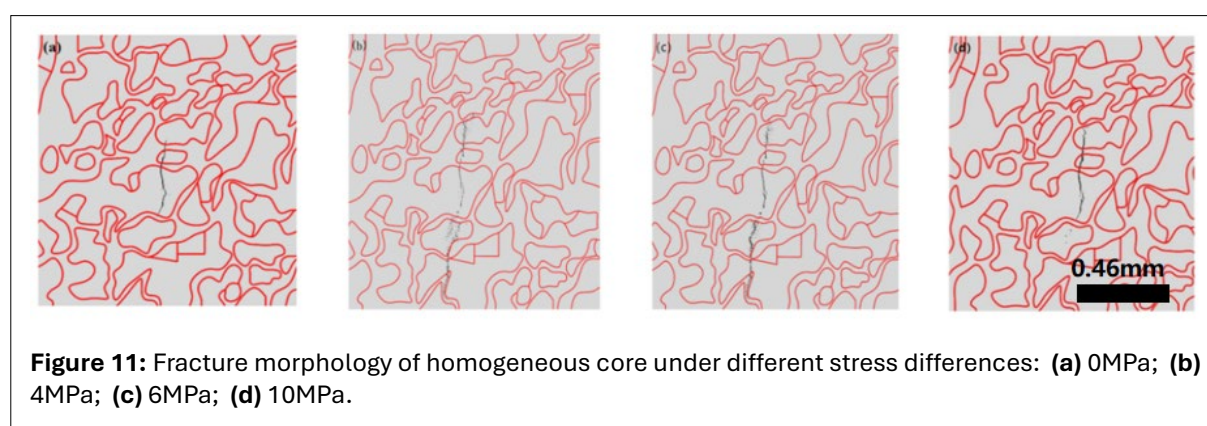
4.2.3. Sensitivity analyses of the stress difference

We further added two more groups of stresses (4 Mpa with 6 Mpa on the X direction and 10 Mpa on the Y direction; 6 Mpa with 4 Mpa on the X direction and 10 Mpa on the Y direction) to illustrate the sensitivity of the stress difference. **Figure 11** and **Figure 12** show the changes of fracture morphology with the stress difference in the homogeneous and the heterogeneous cores, respectively.
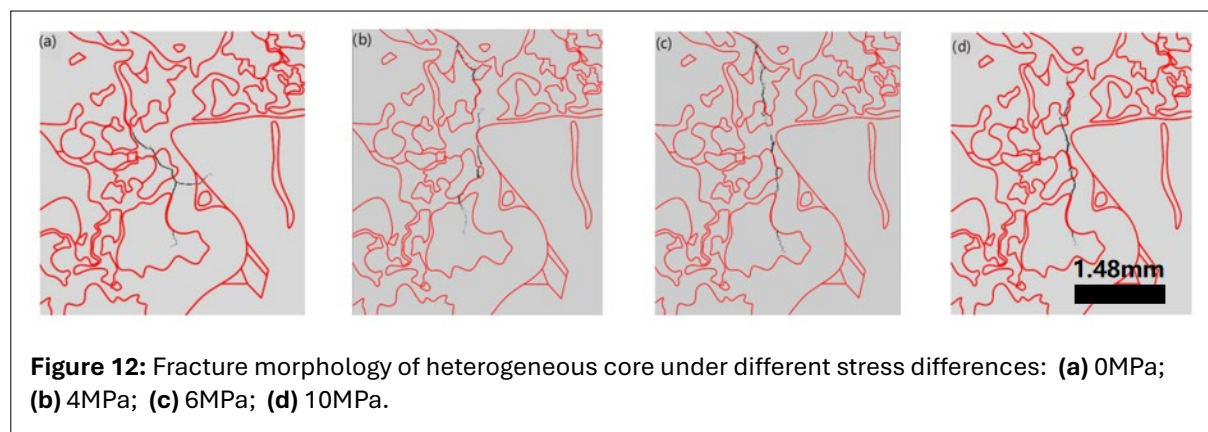
For the homogeneous core, the stress difference has little impact on its fracture morphology, as all the fractures penetrate the gravel without significant differences except for some slight local deflections. However, the stress difference does impact the fracture morphology in the heterogeneous core. When the stress difference is small, the heterogeneous rock properties dominate, while for larger stress differences, the stress boundaries dominate. Therefore, the fracture evolution in the heterogeneous core changes from deflection to penetration mode with the increase in the stress difference.

4.3.   The differences in fracture propagation length and velocity

4.3.1. Comparisons of fracture length & propagation velocity under a stress difference of 10 MPa
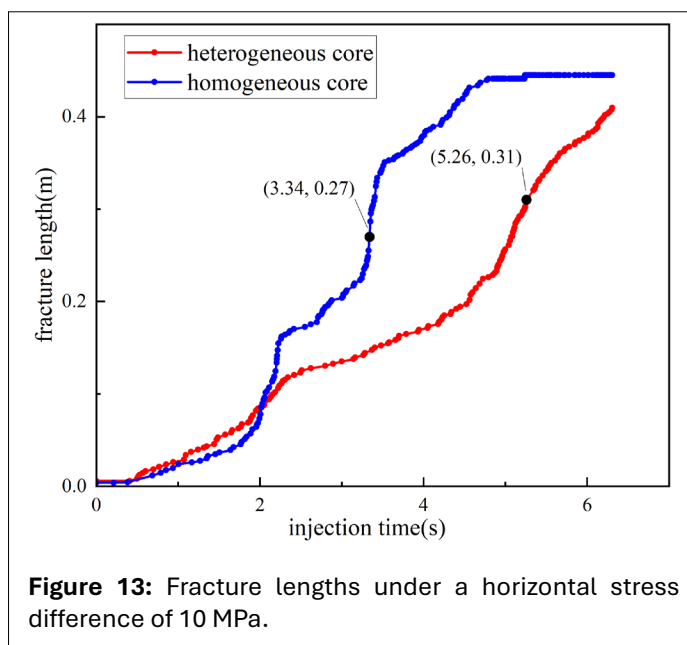
Figure 11 presents the comparison of fracture lengths in homogeneous and heterogeneous core models under a horizontal stress difference of 10 MPa (model parameters as provided in **Table 4**). The results indicate that variations in gravel shape and mechanical properties significantly affect the final fracture length, with the fracture in the homogeneous core being longer than that in the heterogeneous core.

Figure 11: Fracture morphology of homogeneous core under different stress differences: **(a)** 0MPa; **(b)** 4MPa; **(c)** 6MPa; **(d)** 10MPa.

Figure 12: Fracture morphology of heterogeneous core under different stress differences: **(a)** 0MPa; **(b)** 4MPa; **(c)** 6MPa; **(d)** 10MPa.

This phenomenon suggests that the heterogeneity of conglomerate reservoirs increases the difficulty of hydraulic fracture propagation.
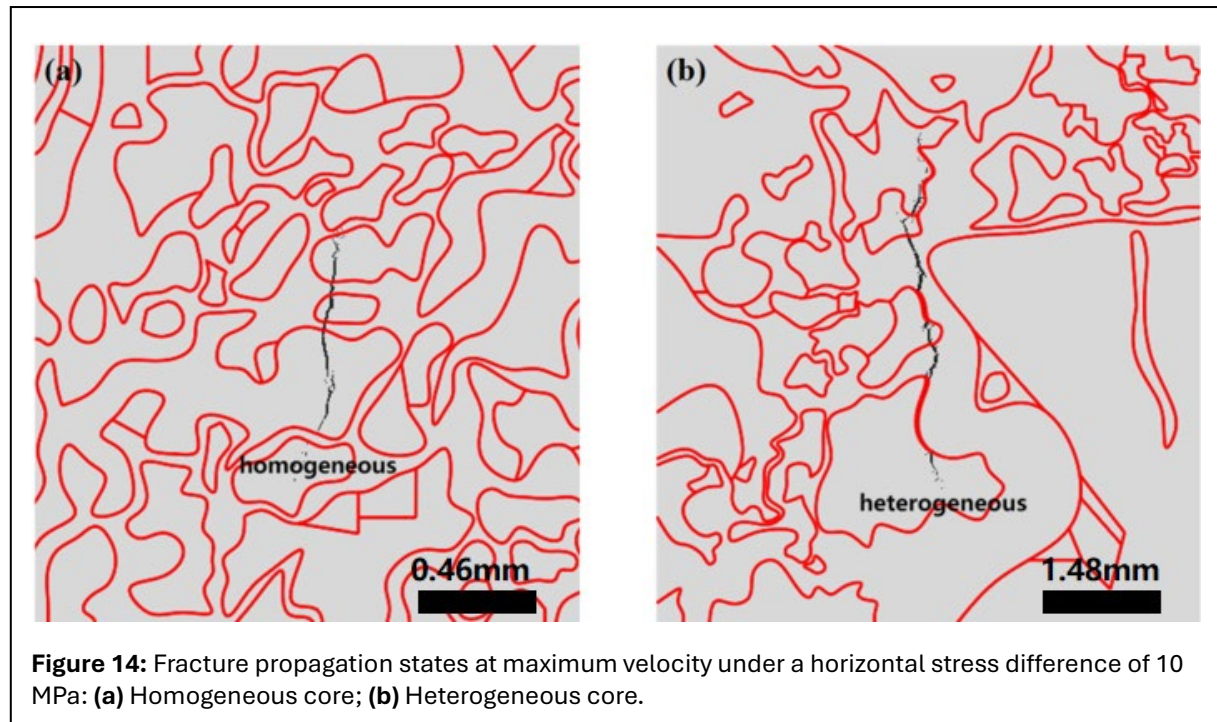
Figure 13 highlights the specific coordinates where the fracture propagation velocity reaches its peak for both homogeneous and heterogeneous core models, while **Figure 14** illustrates the corresponding fracture propagation states at these peak coordinates. The results show that the peak propagation velocity for both cores occurs when the fracture first encounters the gravel interface; however, significant differences are observed between the two cases. In the homogeneous core, the maximum propagation velocity of 1.65 m/s is reached at 3.3 seconds, whereas in the heterogeneous core, the maximum velocity of 0.70 m/s is reached at 5.3 seconds. The peak velocity in the homogeneous core significantly exceeds that in the heterogeneous core. These findings further demonstrate that reservoir heterogeneity significantly hinders fracture propagation velocity.

Figure 13: Fracture lengths under a horizontal stress difference of 10 MPa.

4.3.2. Comparisons of fracture length& propagation velocity under a stress difference of 0 MPa

Figure 15 compares the fracture lengths in homogeneous and heterogeneous core models under a horizontal stress difference of 0 MPa. Due to fracture bifurcation in the heterogeneous core (as shown in **Fig. 12**), the conclusion regarding fracture length differs from that of **Figure 13**. In this case, the final fracture lengths of the homogeneous and heterogeneous cores are nearly identical. However, as shown in **Figure 15**, the hydraulic fracture length in the homogeneous core remains greater than that in the heterogeneous core throughout most of the propagation process. This observation further highlights the hindering effect of heterogeneity on fracture propagation.

In **Figure 15**, black dots indicate the coordinates where the fracture propagation velocity reaches its maximum for both homogeneous and heterogeneous core models, while **Figure 16** displays the corresponding fracture propagation images at these peak coordinates. The results show that the homogeneous core achieves its maximum propagation velocity of 0.9 m/s at 2.7 seconds when the fracture penetrates the gravel and contacts the interface. In contrast, the heterogeneous core reaches its maximum velocity of 0.29 m/s at 5.2 seconds, just as the fracture begins to contact the interface. This finding is consistent with the results of **Figure 16**, confirming that for both homogeneous and

Figure 14: Fracture propagation states at maximum velocity under a horizontal stress difference of 10 MPa: **(a)** Homogeneous core; **(b)** Heterogeneous core.

heterogeneous cores, the maximum hydraulic fracture velocity occurs when the fracture first contacts the interface.

Furthermore, it is noteworthy that under a horizontal stress difference of 0 MPa, the maximum fracture propagation velocity for both homogeneous and heterogeneous cores is lower than that observed under a stress difference of 10 MPa. This result indicates that, in addition to rock heterogeneity, the stress state also plays a significant role in influencing hydraulic fracture propagation.

Figure 15: Fracture lengths under a horizontal stress difference of 0 MPa.

Figure 16: Fracture propagation status at maximum velocity under a horizontal stress difference of 0 MPa: **(a)** Homogeneous core; **(b)** Heterogeneous core.
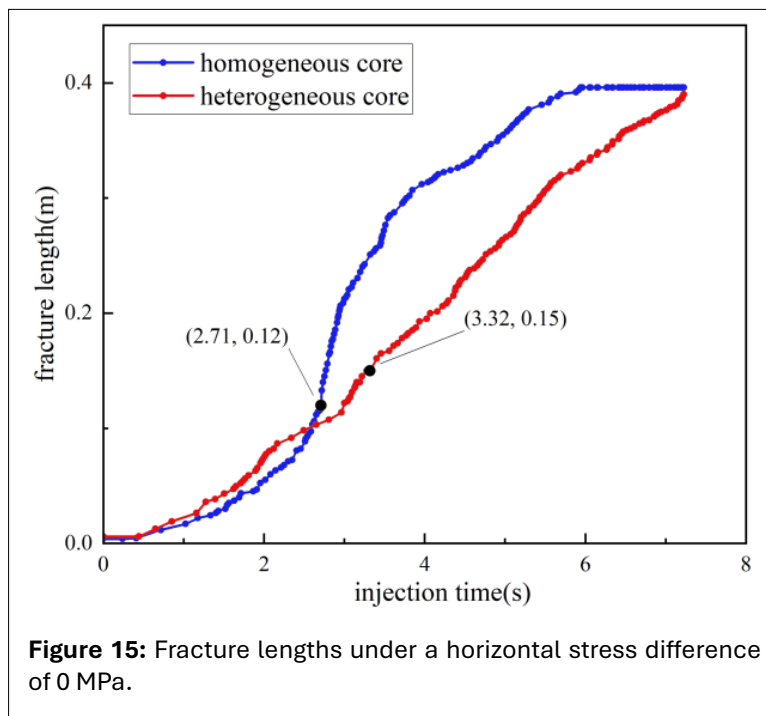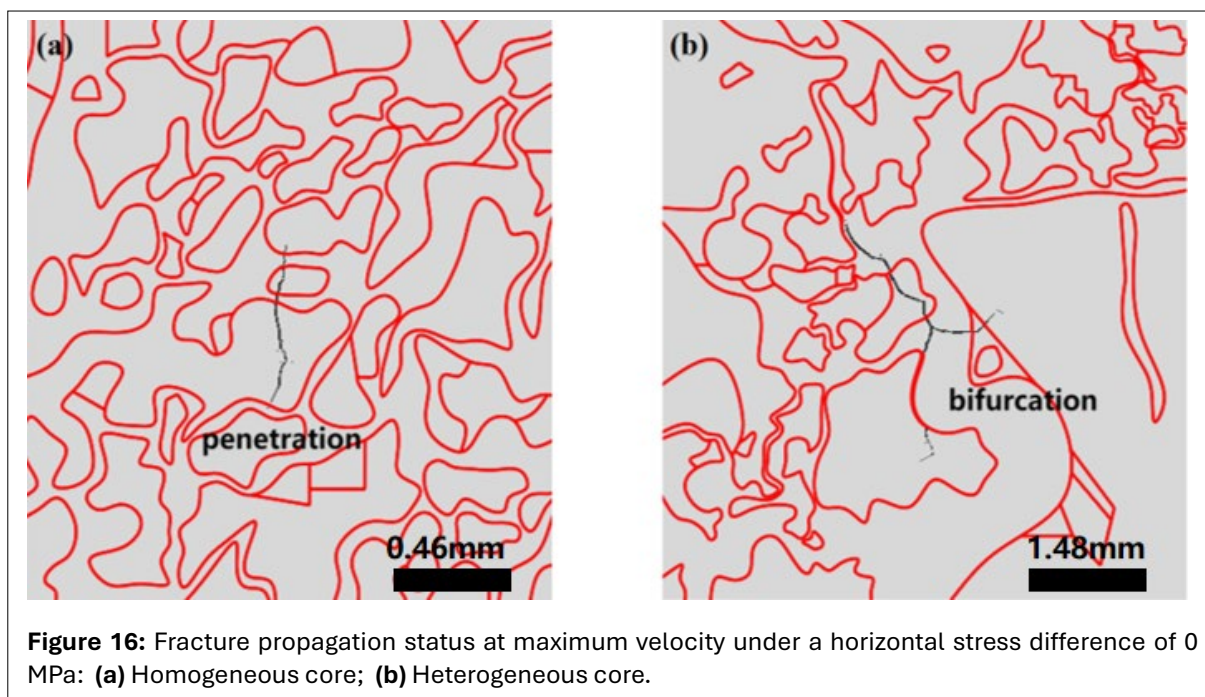
5.   CONCLUSION

This paper models the hydraulic fracture propagation processes in real conglomerate cores from the Mahu oilfield in Xinjiang, China. A finite element hydraulic fracturing model based on the GPPCZ method was developed, incorporating the heterogeneous characteristics of conglomerates, such as structure, mineral composition, and mineral distribution. The model's accuracy was validated by comparing the results with experimental data. Comparison with experimental results shows that hydraulic fractures extend along the principal stress direction. On the left side, the fractures penetrate the gravel, while on the right side, they deflect around the gravel, thus validating the accuracy of the model. Two representative real conglomerate samples from the Mahu oilfield are selected for hydraulic fracturing simulation analysis. The homogeneous core has a porosity of 0.141, whereas the heterogeneous core has a relatively lower porosity of 0.097. QEMSCAN mineral composition analysis reveals that the homogeneous core contains 40.41% quartz and 24.9% albite, while the heterogeneous core has a significantly higher quartz content of 61.63% and a lower albite content of 16.86%. Additionally, the heterogeneous core exhibits mixed gravel structural features with various minerals including quartz-albite-illite mixed gravel and illite-kaolinite mixed gravel, which are absent in the homogeneous core. We compare the morphology and propagation rate of the hydraulic fractures in the homogeneous and heterogeneous core models. The results indicate that:

a) **Under a stress difference of 10 MPa**, the fracture in the homogeneous core propagates along a straight path, whereas the fracture in the heterogeneous core exhibits deflection at gravel interfaces and undergoes multiple bifurcations. This indicates that heterogeneity significantly affects the propagation path of hydraulic fractures, particularly at interfaces, where fractures tend to propagate in regions with lower tensile fracture energy.

b) **Under a stress difference of 0 MPa**, the fracture in the homogeneous core propagates in a relatively straight path without any deflection or bifurcation. In contrast, the fracture in the heterogeneous core exhibits inclination and bifurcation at multiple locations, indicating that rock heterogeneity increases the irregularity of fracture propagation.

c) **With increasing stress difference**, the fracture morphology does not change qualitatively in the homogeneous core, while the fracturing pattern changes from the deflection mode to the penetration mode in the heterogeneous core, as the stress boundary constrictions surpass the

inner gravel energy. This suggests that we can adjust field-scale fracturing strategies for heterogeneous reservoirs by changing the confining stress level and direction.

d) The peak fracture propagation velocity for both homogeneous and heterogeneous cores occurs when the fracture first reaches the interface. The peak velocities also demonstrate that the propagation speed in the heterogeneous core is significantly lower than that in the homogeneous core. In the homogeneous core, the fracture quickly reaches its maximum propagation velocity upon contacting the gravel, whereas in the heterogeneous core, the propagation velocity is hindered by heterogeneity, resulting in a delayed and lower peak velocity.

It is worth mentioning that the main scope of this work is to directly compare the fracture developments in real homogeneous and heterogeneous cores at the pore scale, presenting micro-scale details. Future work should focus on upscaling these findings and validating them against field-scale data.

STATEMENTS AND DECLARATIONS

Supplementary Material

Further information on the parameters used and the workflow for the 3D model creation from the CT images can be found in the Supplementary Material, which is available for download here.

Acknowledgements

Author Contributions

Mingyang Zhang: Investigation, Methodology, Validation, Writing – Review & Editing. **Yanying Chen:** Investigation, Writing – Original Draft. **Ming Yue:** Supervision. **Ninghong Jia:** Data Curation. **Weifeng Lyu:** Data Curation. **Amer Alizadeh:** Software. **Haoran Cheng:** Writing – Review & Editing. **Chiyu Xie:** Supervision, Project Administration, Writing – Review & Editing.

Conflicts of Interest

There are no conflicts of interest to declare.

Data, Code & Protocol Availability

The data are available from the corresponding author on reasonable request.

ORCID IDs

Mingyang Zhang   https://orcid.org/0009-0002-2279-6639
Yanying Chen   https://orcid.org/0009-0008-0949-3610
Ming Yue   https://orcid.org/0000-0003-2192-6032
Ninghong Jia   https://orcid.org/0000-0003-1034-6833
Weifeng Lyu   https://orcid.org/0000-0003-0036-7649
Amer Alizadeh   https://orcid.org/0000-0001-9578-2313
Haoran Cheng   https://orcid.org/0000-0002-4284-9235
Chiyu Xie   https://orcid.org/0000-0002-2813-6925

REFERENCES

1. Alfano, G. (2006). On the influence of the shape of the interface law on the application of cohesive-zone models. *Composites Science and Technology*, 66(6), 723–730. https://doi.org/10.1016/j.compscitech.2004.12.024

2. Cain, A. J., Lemley, C. O., Walters, F. K., Christiansen, D. L., King, E. H., & Hopper, R. M. (2017). Pre-breeding beef heifer management and season affect mid to late gestation uterine artery hemodynamics. *Theriogenology*, 87, 9–15. https://doi.org/10.1016/j.theriogenology.2016.07.031

3. Cao, Y., He, Q., & Liu, C. (2022). Numerical investigation of fracture morphology characteristics in heterogeneous reservoirs. *Processes*, 10(12), 2604. https://doi.org/10.3390/pr10122604

4. Chen, J. (2022). The influence of tensile strength difference with variable gravel sizes on the hydraulic fracture propagation in the conglomerate reservoir. *Geofluids*, 2022, 1–9. https://doi.org/10.1155/2022/5290189

5. Chen, Z., Bunger, A. P., Zhang, X., & Jeffrey, R. G. (2009). Cohesive zone finite element-based modeling of hydraulic fractures. *Acta Mechanica Solida Sinica*, 22(5), 443–452. https://doi.org/10.1016/S0894-9166(09)60295-0

6. Choupani, N. (2008). Mixed-mode cohesive fracture of adhesive joints: Experimental and numerical studies. *Engineering Fracture Mechanics*, *75*(15), 4363–4382. https://doi.org/10.1016/j.engfracmech.2008.04.023

7. Chu, S., & Majumdar, A. (2012). Opportunities and challenges for a sustainable energy future. *Nature*, 488(7411), 294–303. https://doi.org/10.1038/nature11475

8. Dahi Taleghani, A., Gonzalez-Chavez, M., Yu, H., & Asala, H. (2018). Numerical simulation of hydraulic fracture propagation in naturally fractured formations using the cohesive zone model. *Journal of Petroleum Science and Engineering*, *165*, 42–57. https://doi.org/10.1016/j.petrol.2018.01.063

9. Eshiet, K. I., Sheng, Y., & Ye, J. (2013). Microscopic modelling of the hydraulic fracturing process. *Environmental Earth Sciences*, 68(4), 1169–1186. https://doi.org/10.1007/s12665-012-1818-5

10. Galloway W E, Hobday D K. Terrigenous clastic depositional systems: applications to petroleum, coal, and uranium exploration (M). Springer Science & Business Media, 2012.

11. He M, Han Z, Yang H. (2019). Molecular dynamics simulation of deformation and failure mechanism of kaolinite at different temperatures. Journal of Mining Science and Technology, 4: 8-16, https://dx.doi.org/10.19606/j.cnki.jmst.2023.03.006

12. He, J., Tang, H., Wang, L., Yang, Z., Wang, Y., Zhang, X., Hu, Q., & Wan, B. (2021). Genesis of heterogeneity in conglomerate reservoirs: Insights from the Baikouquan formation of Mahu sag, in the Junggar Basin, China. *Petroleum Science and Technology*, 39(1), 11–29. https://doi.org/10.1080/10916466.2020.1830107

13. Hu, X.-C., Ding, X.-Z., Su, G.-S., & Liao, M.-P. (2022). Effect of cleavage characteristics of mineral grains on the failure process of hard rock based on UDEC-GBM modeling. *Chinese Journal of Engineering*, 44(7), 1160–1170. https://doi.org/https://doi.org/10.13374/j.issn2095-9389.2020.12.10.002

14. Jia, H., Ji, H., Wang, L., Gao, Y., Li, X., & Zhou, H. (2017). Reservoir quality variations within a conglomeratic fan-delta system in the Mahu sag, northwestern Junggar Basin: Characteristics and controlling factors. *Journal of Petroleum Science and Engineering*, 152, 165–181. https://doi.org/10.1016/j.petrol.2017.03.002

15. Lei, Z., Dou, X., Wang, Q., Wang, R., Ji, D., Chen, Z., & Xing, G. (2025). A semi-analytical model of a hydraulically fractured horizontal well with pre-darcy flow and stimulated reservoir volume in a radial composite shale reservoir. *SPE Journal*, 30(02), 743–761. https://doi.org/10.2118/223942-PA

16. Li, J., Tang, Y., Wu, T., Zhao, J., Wu, H., Wu, W., & Bai, Y. (2020). Overpressure origin and its effects on petroleum accumulation in the conglomerate oil province in Mahu Sag, Junggar Basin, NW China. *Petroleum Exploration and Development*, 47(4), 726–739. https://doi.org/10.1016/S1876-3804(20)60088-X

17. Li, M., Tang, S., Guo, T., & Qi, M. (2018). Numerical investigation of hydraulic fracture propagation in the glutenite reservoir. *Journal of Geophysics and Engineering*, 15(5), 2124–2138. https://doi.org/10.1088/1742-2140/aaba27

18. Li, X., Gu, K., Xu, W., Song, J., Pan, H., et al. (2023). Effects of pore water content on stress sensitivity of tight sandstone oil reservoirs: A study of the Mahu block (Xinjiang province, China). *Processes*, 11(11), 3153. https://doi.org/10.3390/pr11113153

19. Li, Y., Deng, J. G., Liu, W., & Feng, Y. (2017). Modeling hydraulic fracture propagation using cohesive zone model equipped with frictional contact capability. *Computers and Geotechnics*, 91, 58–70. https://doi.org/10.1016/j.compgeo.2017.07.001

20. Liravi, F., Das, S., & Zhou, C. (2015). Separation force analysis and prediction based on cohesive element model for constrained-surface Stereolithography processes. *Computer-Aided Design*, 69, 134–142. https://doi.org/10.1016/j.cad.2015.05.002

21. Liu, P., Lou, F., Du, J., Chen, X., Liu, J., & Wang, M. (2023). Impact of key parameters on far-field temporary plugging and diverting fracturing in fractured reservoirs: A 2D finite element study. *Advances in Geo-Energy Research*, 10(2), 104–116. https://doi.org/10.46690/ager.2023.11.05

22. Luo, S., Zhao, Y., Zhang, L., Chen, Z., & Zhang, X. (2021). Integrated simulation for hydraulic fracturing, productivity prediction, and optimization in tight conglomerate reservoirs. *Energy & Fuels*, 35(18), 14658–14670. https://doi.org/10.1021/acs.energyfuels.1c02161

23. Ma, X., Zou, Y., Li, N., Chen, M., Zhang, Y., & Liu, Z. (2017). Experimental study on the mechanism of hydraulic fracture growth in a glutenite reservoir. *Journal of Structural Geology*, 97, 37–47. https://doi.org/10.1016/j.jsg.2017.02.012

24. May, M., & Hallett, S. R. (2010). A combined model for initiation and propagation of damage under fatigue loading for cohesive interface elements. *Composites Part A: Applied Science and Manufacturing*, 41(12), 1787–1796. https://doi.org/10.1016/j.compositesa.2010.08.015

25. Mohammadnejad, T., & Khoei, A. R. (2013). An extended finite element method for hydraulic fracture propagation in deformable porous media with the cohesive crack model. *Finite Elements in Analysis and Design*, 73, 77–95. https://doi.org/10.1016/j.finel.2013.05.005

26. Pan, Y., Ma, X., Li, J., Xie, B., & Xiong, D. (2023). Numerical simulation of hydraulic fracture propagation in conglomerate reservoirs: A case study of mahu oilfield. *Processes*, 11(7), 2073. https://doi.org/10.3390/pr11072073

27. Qiang S, Chunlu J, Shuyun Z. Water stability test and mechanical property of water saturated rocks (2011). Journal of Mining & Safety Engineering, 2011, 28(2): 236-240. https://kns.cnki.net/kcms2/article/abstract?v=djJQIkjC3sBHNxmvKh1rKU0V4RvWBzvMuNGlU0yvsGOZ4AV4NZ_GfAUuL1zihl2XilC61JUw9zjF7uLI96d6tBMbwYREhBNXkEGRxc5IE6GEPTjmiCSPZa6voC_8yCOoVOYeRd6_3G0d57raZw65G132v2mkJBLH&uniplatform=NZKPT

28. Qinghui, L., Mian, C., Bing, H., & Jiazhen, Z. (2012). Rock mechanical properties and brittleness evaluation of shale gas reservoir. *Petroleum Drilling Techniques*, 40(4), 17–22. https://doi.org/https://dx.doi.org/10.3969/j.issn.1001-0890.2012.04.004

29. Ren, L., Zhu, Z., Yang, Q., & Ai, T. (2013). Investigation on the applicability of several fracture criteria to the mixed mode brittle fractures. *Advances in Mechanical Engineering*, 5, 545108. https://doi.org/10.1155/2013/545108

30. Rui, Z., Guo, T., Feng, Q., Qu, Z., Qi, N., & Gong, F. (2018). Influence of gravel on the propagation pattern of hydraulic fracture in the glutenite reservoir. *Journal of Petroleum Science and Engineering*, 165, 627–639. https://doi.org/10.1016/j.petrol.2018.02.067

31. Shi, X., Qin, Y., Xu, H., Feng, Q., Wang, S., Xu, P., & Han, S. (2021). Numerical simulation of hydraulic fracture propagation in conglomerate reservoirs. *Engineering Fracture Mechanics*, 248, 107738. https://doi.org/10.1016/j.engfracmech.2021.107738

32. Song, Z., Song, Y., Li, Y., Bai, B., Song, K., & Hou, J. (2020). A critical review of CO_2 enhanced oil recovery in tight oil reservoirs of North America and China. *Fuel*, 276, 118006. https://doi.org/10.1016/j.fuel.2020.118006

33. Sun, J., You, X., Zhang, Q., Xue, J., & Chang, Q. (2023). Development characteristics and genesis of deep tight conglomerate reservoirs of Mahu area in Junggar Basin, China. *Journal of Natural Gas Geoscience*, 8(3), 201–212. https://doi.org/10.1016/j.jnggs.2023.05.001

34. Tang H, Liang H, Zhang L, et al. Hydraulic fracture extension patterns of conglomerate reservoirs and relevant influencing factors. (2022). Acta Petrolei Sinica, 2022, 43(6): 871. https://www.syxb-cps.com.cn/EN/10.7623/syxb202206011

35. Tomac I. Micro-mechanical aspects of hydraulic fracture propagation and proppant flow and transport for stimulation of enhanced geothermal systems–A discrete element study (Monograph). Colorado School of Mines, 2014. https://www.proquest.com/openview/7e0b63af8af69e1d97a5ff4d1dc054cf/1?pq-origsite=gscholar&cbl=18750

36. Wang, D., Dong, Y., Sun, D., & Yu, B. (2020). A three-dimensional numerical study of hydraulic fracturing with degradable diverting materials via CZM-based FEM. *Engineering Fracture Mechanics*, 237, 107251. https://doi.org/10.1016/j.engfracmech.2020.107251

37. Wang, H. (2015). Numerical modeling of non-planar hydraulic fracture propagation in brittle and ductile rocks using XFEM with cohesive zone method. *Journal of Petroleum Science and Engineering*, 135, 127–140. https://doi.org/10.1016/j.petrol.2015.08.010

38. Wang, H. (2019). Hydraulic fracture propagation in naturally fractured reservoirs: Complex fracture or fracture networks. *Journal of Natural Gas Science and Engineering*, 68, 102911. https://doi.org/10.1016/j.jngse.2019.102911

39. Wang, J., Ge, H., Liu, J., Shen, Y., Zhang, Z., Luo, S., & Liu, D. (2022). Effects of gravel size and content on the mechanical properties of conglomerate. *Rock Mechanics and Rock Engineering*, 55(4), 2493–2502. https://doi.org/10.1007/s00603-021-02760-0

40. Wang, Z., Lin, B., Chen, G., Dai, Y., & Chen, A. (2023). Experimental study on evaluation of conglomerate reservoir support-type fracture conductivity in Xinjiang oilfield. *Energy*, 278, 127877. https://doi.org/10.1016/j.energy.2023.127877

41. Wu, S., Yu, C., Hu, X., Yu, Z., & Jiang, X. (2022). Characterization of mineral and pore evolution under CO_2-brine-rock interaction at in-situ conditions. *Advances in Geo-Energy Research*, 6(2), 177–178. https://doi.org/10.46690/ager.2022.02.09

42. Xi, X., Shipton, Z. K., Kendrick, J. E., Fraser-Harris, A., Mouli-Castillo, J., et al. (2022). Mixed-mode fracture modelling of the near-wellbore interaction between hydraulic fracture and natural fracture. *Rock Mechanics and Rock Engineering*, 55(9), 5433–5452. https://doi.org/10.1007/s00603-022-02922-8

43. Xi, X., Yang, S., Li, C.-Q., Cai, M., Hu, X., & Shipton, Z. K. (2018). Meso-scale mixed-mode fracture modelling of reinforced concrete structures subjected to non-uniform corrosion. *Engineering Fracture Mechanics*, 199, 114–130. https://doi.org/10.1016/j.engfracmech.2018.05.036

44. Xu, Z., Liu, X., & Liang, L. (2022). Numerical investigation of hydraulic fracture propagation morphology in the conglomerate reservoir. *Geofluids*, 2022, 1–22. https://doi.org/10.1155/2022/6811300

45. Yan, X., Mou, J., Tang, C., Xin, H., Zhang, S., et al. (2021). Numerical investigation of major impact factors influencing fracture-driven interactions in tight oil reservoirs: A case study of Mahu Sug, Xinjiang, China. *Energies*, 14(16), 4881. https://doi.org/10.3390/en14164881

46. Yang, Q., & Cox, B. (2005). Cohesive models for damage evolution in laminated composites. *International Journal of Fracture*, 133(2), 107–137. https://doi.org/10.1007/s10704-005-4729-6

47. Yang T. Research on micromechanical properties of breccia based on atomic force microscope (J). Fly Ash Comprehensive Utilization, 2022, 36 (03): 29-35. 10.19860/j.cnki.issn1005-8249.2022.03.006

48. Yu, Z., Wang, Z., Jiang, Q., Wang, J., Zheng, J., & Zhang, T. (2022). Analysis of factors of productivity of tight conglomerate reservoirs based on random forest algorithm. *ACS Omega*, 7(23), 20390–20404. https://doi.org/10.1021/acsomega.2c02546

49. Zeng, Y., Cheng, W., Zhang, X., & Xiao, B. (2020). A criterion for identifying a mixed-mode I/II hydraulic fracture crossing a natural fracture in the subsurface. *Energy Exploration & Exploitation*, 38(6), 2507–2520. https://doi.org/10.1177/0144598720923781

50. Zhang, B., Guo, T., Chen, M., Xue, L., Zhang, Y., et al. (2024). Experimental research on hydraulic fracture evolution characteristics of multi-well pad fracturing in a tight conglomerate reservoir. *Engineering Fracture Mechanics*, 312, 110609. https://doi.org/10.1016/j.engfracmech.2024.110609

51. Zhang, Z., Zhang, S., Shi, S., Zou, Y., Li, J., et al. (2022). Evaluation of multi-scale mechanical properties of conglomerate using nanoindentation and homogenization methods: A case study on tight conglomerate reservoirs in southern slope of Mahu sag. *Chinese Journal of Rock Mechanics and Engineering*, 41(5), 926–940. https://doi.org/10.13722/j.cnki.jrme.2021.1186

52. Zhao, Y., Wang, L., Ma, K., & Zhang, F. (2022). Numerical simulation of hydraulic fracturing and penetration law in continental shale reservoirs. *Processes*, 10(11), 2364. https://doi.org/10.3390/pr10112364

53. Zhao, Y., Zhu, G., Dong, Y., Danesh, N. N., Chen, Z., & Zhang, T. (2017). Comparison of low-field NMR and microfocus X-ray computed tomography in fractal characterization of pores in artificial cores. *Fuel*, 210, 217–226. https://doi.org/10.1016/j.fuel.2017.08.068

54. Zhu, D., Zhang, L., Song, X., Lian, H., & Niu, D. (2023). Propagation mechanism of the hydraulic fracture in layered-fractured-plastic formations. *International Journal of Fracture*, 241(2), 189–210. https://doi.org/10.1007/s10704-023-00694-y

55. Zhu, W., Chen, Z., He, X., Liu, J., Guo, S., et al. (2024). Numerical analysis of the dynamic mechanisms in hydraulic fracturing with a focus on natural fractures. *Journal of Geophysical Research: Solid Earth*, 129(12), e2024JB029487. https://doi.org/10.1029/2024JB029487

56. Zhu, W., Chen, Z., He, X., Tian, Z., & Wang, M. (2023). Numerical investigation of influential factors in hydraulic fracturing processes using coupled discrete element-lattice Boltzmann method. *Journal of Geophysical Research: Solid Earth*, 128(9), e2023JB027292. https://doi.org/10.1029/2023JB027292

57. Zhuang, L., & Zang, A. (2021). Laboratory hydraulic fracturing experiments on crystalline rock for geothermal purposes. *Earth-Science Reviews*, *216,* 103580. https://doi.org/10.1016/j.earscirev.2021.103580